

# Homogeneous Decomposition Mechanisms of Diethylzinc by Raman Spectroscopy and Quantum Chemical Calculations

Young Seok Kim,<sup>†</sup> Yong Sun Won,<sup>†</sup> Helena Hagelin-Weaver,<sup>†</sup> Nicoló Omenetto,<sup>‡</sup> and Tim Anderson<sup>\*,†</sup>

Department of Chemical Engineering and Department of Chemistry, University of Florida, Gainesville, Florida 32611

Received: October 26, 2007; In Final Form: December 19, 2007

The gas-phase decomposition pathways of diethylzinc (DEZn), a common precursor for deposition of Zn–VI compounds, were investigated in detail. The homogeneous thermal decomposition of DEZn in N<sub>2</sub> carrier was followed in an impinging-jet, up-flow reactor by Raman scattering. Density Functional Theory calculations were performed to describe the bond dissociation behavior using the model chemistry B3LYP/6-311G(d) to estimate optimal geometries and Raman active vibrational frequencies of DEZn, as well as anticipated intermediates and products. Comparison of the measured DEZn decomposition profile to that predicted by a 2-D hydrodynamic simulation revealed that simple bond dissociation between zinc and carbon atoms is the dominant homogeneous thermal decomposition pathway. The calculations suggest several reactions involving intermediates and Raman scattering experiments confirming the formation of the dimer (ZnC<sub>2</sub>H<sub>5</sub>)<sub>2</sub>. In a different set of experiments, photolysis of DEZn gave evidence for decomposition by  $\beta$ -hydride elimination. The results suggest that  $\beta$ -hydride elimination is a minor pathway for the gas-phase homogeneous pyrolysis of diethylzinc. A reasonable transition state during  $\beta$ -hydride elimination was identified, and the calculated energies and thermodynamic properties support the likelihood of these reaction steps.

## 1. Introduction

Several applications motivate chemical vapor deposition (CVD) of Zn-containing thin films. In particular, the Zn–VI compound semiconductors and alloys with other group II–VI compounds are used as the host semiconductor material in a variety of optoelectronic devices including light emitting devices, photodetectors, and lasers.<sup>1–3</sup> Among these compound semiconductors, zinc oxide is commonly used as a transparent conducting material in emissive device applications as well as solar cells.<sup>4–8</sup> ZnO can be made highly conductive by adjusting the oxygen vacancy concentration or doping (e.g., Al), whereas recent reports of p-type conductivity are encouraging for transparent electronics.<sup>9,10</sup> Thin films of Zn-containing compound semiconductors have been deposited by CVD from a variety of organo-Zn precursors, but most commonly from Zn-(C<sub>2</sub>H<sub>5</sub>)<sub>2</sub>. Because deposition takes place at an elevated temperature, typically in the range 300–600 °C, homogeneous thermal decomposition can be important in the reaction pathway. The multiple early studies of Et<sub>2</sub>Zn homogeneous decomposition have suggested Zn–C bond homolysis as the dominant initial decomposition step,<sup>11–14</sup> primarily on the basis of the indirect evidence of *n*-C<sub>4</sub>H<sub>10</sub> detection. A later laser pyrolysis investigation by Linney and Russel,<sup>15</sup> however, did not observe *n*-C<sub>4</sub>H<sub>10</sub> but did identify ZnH<sub>2</sub> as a wall deposit, which is a direct product of double  $\beta$ -hydride elimination of Et<sub>2</sub>Zn. The aim of this study to quantitatively probe the rate of disappearance of Et<sub>2</sub>Zn as well as search for direct reaction products in an inverted, impinging-jet test reactor coupled to a Raman spectrometer.

The first detailed study of Et<sub>2</sub>Zn pyrolysis was reported by Koski et al.<sup>11</sup> using the toluene carrier method. They suggested

that sequential homolytic fission of the metal–carbon bond is the dominant dissociation mechanism (reactions 1a and 1b) on the basis of the observation. Jackson subsequently investigated the onset of pyrolysis of diethylzinc in H<sub>2</sub> and He flows by optical monitoring of the rate of condensation of Zn.<sup>12</sup> More recently, Dumont et al. used mass spectroscopic analysis with capillary sampling at a single point near the heated susceptor of a pedestal reactor to study the decomposition of Zn(C<sub>2</sub>H<sub>5</sub>)<sub>2</sub> in both He and H<sub>2</sub>.<sup>13,14</sup> These researchers also observed ethane and *n*-butane as the predominant decomposition products. On the basis of their results as well as those of previous studies, Dumont and co-workers also concluded that decomposition was mainly homolytic in nature, with the resultant ethyl radicals undergoing either recombination to yield butane (reaction 1c), disproportionation to yield ethane and ethene (reaction 1d), or decomposition to yield ethane (reaction 1e). Subsequent investigations by others have supported the following decomposition mechanism:

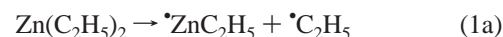


Table 1 summarizes the estimated apparent activation energy for the first order disappearance of Et<sub>2</sub>Zn, presumably by homolytic fission of the first Zn–C bond of DEZn.<sup>11–14</sup> It is noted that the measured activation energy in each study is based

\* Corresponding author. E-mail: tim@ufl.edu.

<sup>†</sup> Department of Chemical Engineering.

<sup>‡</sup> Department of Chemistry.

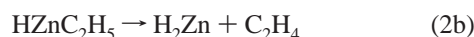
**TABLE 1: Reported Activation Energy for the Homogeneous Dissociation of the First Zn–C Bond of Diethylzinc**

| activation energy [kcal/mol] | frequency factor [s <sup>-1</sup> ] | temp range [°C]  | anal. method                           | ref |
|------------------------------|-------------------------------------|------------------|--|-----|
| 50                           | 10 <sup>9–10</sup>                  | 396–489          | gas chromatography                     | 11  |
| 52.4                         |                                     | 270 <sup>a</sup> | mass spectroscopy                      | 12  |
| 56                           |                                     | 280–520          | mass spectroscopy                      | 13  |
| 52                           | 2 × 10 <sup>16</sup>                | 230–470          | mass spectroscopy using D <sub>2</sub> | 14  |

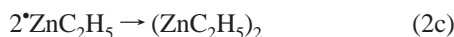
<sup>a</sup> Range not reported, only average measurement temperature.

on direct measurement of the concentration decrease of diethylzinc and indirectly the increase of the <sup>•</sup>C<sub>2</sub>H<sub>5</sub> radical concentration. Experimental detection of the primary reaction intermediate, <sup>•</sup>ZnC<sub>2</sub>H<sub>5</sub>, however, has not been reported, presumably because the lifetimes are too short. Molecular simulations of <sup>•</sup>ZnC<sub>2</sub>H<sub>5</sub> decomposition reported in this work support the presumption that <sup>•</sup>ZnC<sub>2</sub>H<sub>5</sub> has a short lifetime. As listed in Table 1 the reported activation energy for homolysis of the first Zn–C bond is in the range 50–56 kcal/mol, which is considered relatively good agreement among the different measurements. The only evidence supporting sequential homolysis is the detection of ethane and n-butane in the outlet of a MOCVD reactor, neither of which is direct reaction intermediate (i.e., <sup>•</sup>ZnC<sub>2</sub>H<sub>5</sub>) and thus potentially misleading.

In contrast to the bond homolysis radical mechanism suggested above, Linney and Russel<sup>15</sup> observed a different reaction pathway using IR laser-powered homogeneous pyrolysis. They detected H<sub>2</sub>Zn by FTIR and <sup>1</sup>H NMR spectroscopy as the major Zn product of Et<sub>2</sub>Zn homogeneous pyrolysis in the temperature range 280 to 520 °C. This observation and no detection of n-butane led these researchers to conclude double β-hydride elimination as the most probable route (reactions 2a and 2b).



The possibility of heterogeneous reaction contributions and uncertainty in reaction temperature further complicates the comparison of previous work. To better understand the homogeneous pyrolysis mechanism of Zn(C<sub>2</sub>H<sub>5</sub>)<sub>2</sub>, its decomposition was studied by Raman spectroscopy in an translatable impinging-jet reactor. The advantages of Raman scattering are its high spatial resolution and in situ temperature measurement; however, the relatively low sensitivity for species detection is a drawback. Furthermore, scattering cross-sections are required for quantitative analysis. The reactor design used in this study includes a sweep flow to eliminate reactions with walls and limit them only to the heated pedestal. Quantum chemical calculations were used to estimate Raman frequencies to assist in the interpretation of the experimental data. Based on experimental observations and computational results reported here, the following additional reaction step of dimer formation is suggested.



## 2. Experimental and Calculation Details

Except for preliminary experiments using a commercial flow cell reactor (56 cm<sup>3</sup> volume) to measure the Raman scattering cross-section of DEZn, a custom impinging jet reactor was used to study the gas-phase decomposition of Zn(C<sub>2</sub>H<sub>5</sub>)<sub>2</sub> as schematically shown in Figure 1. The organometallic precursor in a

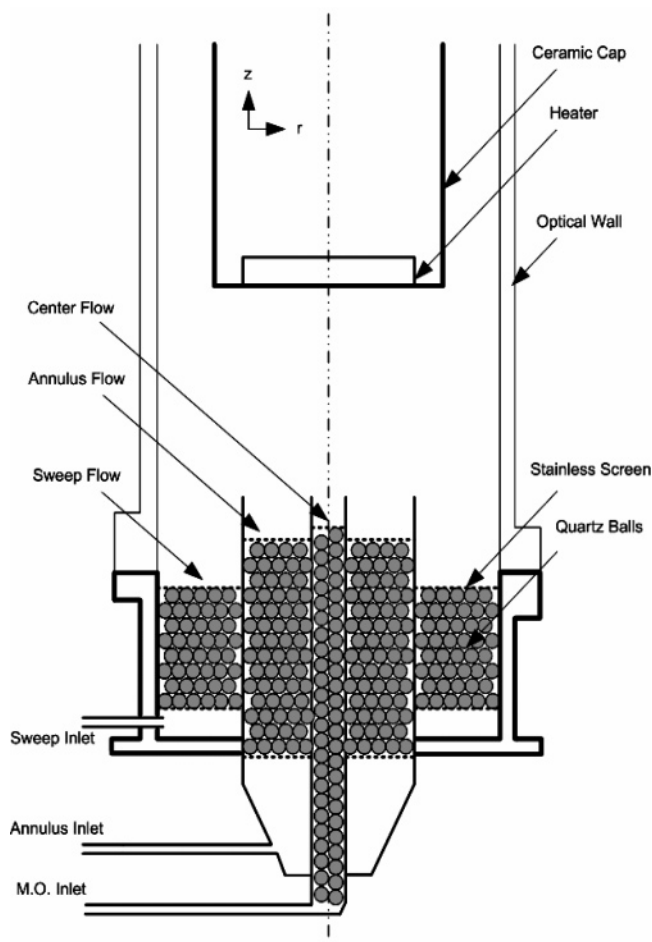


**Figure 1.** Up-flow, impinging-jet reactor for *in-situ* Raman scattering measurements.

carrier gas is introduced through a center-lined tube, while a N<sub>2</sub> sweeping gas flow envelops the organometallic gas to minimize wall deposition of precursors or reaction products. The reactor body is constructed of four optically flat quartz plates fused on edge to produce a square base. A quartz tube with four vertical slits is inserted into this rectangular chamber to provide a better defined flow pattern to simplify modeling. The vertical slits in the tube permit access of the probe beam to the reactor centerline and detection of the scattered light. The up-flowing gas stream impinges on a resistance-heated pedestal susceptor equipped with a control and measurement thermocouple.

Before measuring the concentration and temperature profiles along the centerline of the reactor, a steady-state flow pattern is first established. To ensure that no closed streamlines exist in the reactor, a CH<sub>4</sub> tracer flow study was performed to delineate suitable conditions.<sup>16</sup> This impinging jet reactor was designed to eliminate wall reactions and produce a well defined and easily modeled flow region. The temperature and species concentration gradients that develop along the centerline allow study of reactions over a wide range of conditions in a single steady-state experiment. By adjusting the temperature and gas velocity, the reaction mechanism could be programmed for a homogeneous decomposition study. A more detail description of the reactor as well as the data analysis is given elsewhere.<sup>16</sup>

A U-1000 Raman spectrometer (Jobin Yvon) was used to collect and analyze the scattered light. The 488 nm wavelength of an Ar-ion laser or the frequency doubled 532 nm wavelength of a Nd/YAG solid-state laser was used as the excitation source

and a photomultiplier tube was used as a detector. A maximal laser power of 1–5 W was used, although the actual excitation power was lower due to losses from mirrors and other optical components. A charge-coupled device (CCD) was also available in system but the analytical measurements were mainly performed using the PMT.

The theory of Raman scattering based on fundamental molecular motions, including electronic, rotational, and vibrational motions is very well developed.<sup>17–19</sup> The Raman intensity is inversely proportional to the fourth power of the light source wavelength and to the differential Raman cross-section. To estimate the mole fraction of a specific molecule from the measured intensity, the ratio of the Raman intensity of the molecular species of interest and the carrier gas ( $N_2$ ) is used as shown in

$$x_j = \frac{N_j}{N_j + N_Q} \quad (3)$$

$$\frac{N_Q}{N_j} = \frac{(\tilde{\nu}_0 - \tilde{\nu}_j)^4}{(\tilde{\nu}_0 - \tilde{\nu}_Q)^4} \frac{1 - \exp(-hc\tilde{\nu}_Q/k_B T)}{1 - \exp(-hc\tilde{\nu}_j/k_B T)} \frac{I_Q}{I_j} \sum_j \quad (4)$$

where  $N_j$  and  $I_j$  are the number density and measured intensity of component  $j$ , and the subscript “Q” denotes the Q-branch of  $N_2$  carrier gas.  $\tilde{\nu}_0$ ,  $\tilde{\nu}_j$  and  $\tilde{\nu}_Q$  are the wavenumbers of the incident light, molecular vibration and Q-branch of  $N_2$  carrier gas. The term  $\sum_j$  is the relative Raman cross-section for vibration mode  $j$ .

The Raman intensity of the molecular species of interest is compared to that of  $N_2$  because  $N_2$  is at high concentration and known to have stable rotational and vibrational motions at reaction conditions. In addition to the vibrational frequency, the relative Raman cross-section,  $\Sigma_k$ , is required. In practice, cross-sections are usually reported relative to that of the Q-branch of  $N_2$  because  $N_2$  has sufficient stability to be an internal standard.<sup>20</sup>

$$\sum_k = \frac{C_k \tilde{\nu}_Q}{C_Q \tilde{\nu}_k} = \frac{(\partial\sigma/\partial\Omega)_k (\tilde{\nu}_0 - \tilde{\nu}_Q)^4}{(\partial\sigma/\partial\Omega)_Q (\tilde{\nu}_0 - \tilde{\nu}_k)^4} \frac{1 - \exp(-hc\tilde{\nu}_Q/k_B T)}{1 - \exp(-hc\tilde{\nu}_k/k_B T)} \quad (5)$$

where  $C_k$  is a constant, which contains specific information on the  $k$ th vibration mode. The relative Raman cross-section shown above is calculated using the Q-branch of the  $N_2$  vibrational motion of  $\tilde{\nu}_Q$ , which appears at 2331  $\text{cm}^{-1}$ . The Raman cross-sections for metalorganic precursors, however, are generally not known.

In a preliminary experiment, the Raman cross-section of DEZn was measured in a commercial flow-cell reactor. In this measurement a steady stream of DEZn (10 mol % in  $N_2$ ), normally at atmospheric pressure, was introduced into the flow-cell reactor at 3.0 cm/s velocity and sufficient time was allowed for the reactor to reach steady state. The contents of the cell were then excited with the 532.08 nm line at 1–3 W and the scattered intensity of the Zn–C stretch at 480  $\text{cm}^{-1}$  was recorded. With repeated measurements at room temperature, the value of the relative Raman cross-section of DEZn was estimated to be 4.2. Although the cross-section of this molecule is lower than that of the group III alkyls (e.g.,  $\Sigma_{\text{TMin}} = 22.3$ ), the signal-to-noise ratio at this concentration was sufficient to quantify the  $\text{Zn}(\text{C}_2\text{H}_5)_2$  concentration from the measured intensity of the 480  $\text{cm}^{-1}$  line.

Coupling the experimental observations with the computational calculations enabled identification of reaction intermedi-

**TABLE 2: Calculated Raman Shift ( $\text{cm}^{-1}$ ) of  $\nu[\text{Zn}-\text{C}]$  and  $\nu[\text{Zn}-\text{H}]$  for Selected Zn-Containing Molecules<sup>a</sup>**

| $\text{Zn}(\text{C}_2\text{H}_5)_2$ | $\nu[\text{Zn}-\text{C}]$  |                           | $\delta[\text{Zn}-\text{C} \ \& \ \text{C}-\text{H}]$ | $\nu[\text{Zn}-\text{C}]$ |
|-------------------------------------|----------------------------|---------------------------|---|---------------------------|
|                                     | $^*\text{ZnC}_2\text{H}_5$ | $\text{HZnC}_2\text{H}_5$ | $\text{HZnC}_2\text{H}_5$                             | $\text{H}_2\text{Zn}$     |
| 486.0                               | 313.1                      | 590.5                     | 666.5   | 1918.9                    |

<sup>a</sup> The frequency values of first three molecules are Zn–C vibrational stretching and the other frequency involved Zn–H rocking motion.

ates and thus suggestion of a decomposition mechanism. The density functional theory (DFT) calculations were performed using the Gaussian 03 package.<sup>20</sup> Bond dissociation energies were calculated using Becke’s three-parameter hybrid exchange functional combined with the Lee–Yang–Parr gradient-corrected correlation functional (B3LYP) and the 6-311G(d) basis set. This method and basis set specify the model chemistry used to calculate molecular optimized geometries, and atomic or molecular properties for the reaction species, i.e., Zn-containing molecules.<sup>21–23</sup> This model chemistry was also used to calculate the Raman active frequencies along with the symmetrical vibrational motions between zinc and carbon or zinc and hydrogen atoms in selected intermediate species. Calculated values of the rotational or vibrational frequencies allowed their partition functions to be evaluated to yield Gibbs energies of possible intermediates to judge which reactions are thermodynamically favored. In identifying reaction intermediates, multiple combinations of different fragments, i.e., reaction intermediates, were tested.

### 3. Results and Discussion

The two gas-phase decomposition reaction pathways reported in the literature can be distinguished by their Zn intermediates. The species Zn and  $^*\text{ZnC}_2\text{H}_5$  are produced from homolytic fission, and  $\text{HZnC}_2\text{H}_5$  and  $\text{ZnH}_2$  result from  $\beta$ -hydride elimination. The first set of experiments was designed to promote the decomposition of  $\text{Zn}(\text{C}_2\text{H}_5)_2$  to a sufficient extent that the Zn intermediates could be detected by Raman scattering. To this end photolysis of  $\text{Zn}(\text{C}_2\text{H}_5)_2$  was carried out using the incident laser at high power in the flow cell. To assist in the peak assignment, DFT calculations were performed to identify vibrational frequencies of candidate reaction intermediates.

Several computational approaches were first tested to represent species in the DEZn system. Among them, the B3LYP level calculation with 6-311G(d) basis set was chosen to describe the nature of bond rupture and analyze the thermodynamic properties based on geometry optimization calculations. The products from carbon–carbon dissociation, i.e.,  $\text{Zn}(\text{C}_2\text{H}_5)_2 \rightarrow (\text{C}_2\text{H}_5)\text{Zn}(\text{CH}_2) + \text{CH}_3$ , were not included because the carbon–carbon bond strength is considerably greater than the zinc–carbon bond strength. This assertion is supported by an analysis using the Wiberg bond index in the natural bond orbital (NBO): Zn–C: 0.4990, C–C: 1.0600, C(next to Zn)–H: 0.9362, and C(next to C)–H: 0.9403. On the basis of the optimal geometries, the symmetry point groups were identified and Raman-active vibrational frequencies in normal modes along with the symmetry groups were obtained.<sup>24</sup> Table 2 summarizes the calculated results.

Atomic Zn was not expected to be detected by Raman spectroscopy because the most probable emission radiates from the excited state ( $^1\text{P}_1^0$ ) to the ground state ( $^1\text{S}_0$ ) with just 1.6 ns lifetime, which is too short to be detected.<sup>25</sup> Therefore, Raman scattering experiments were used to search for the possible decomposition fragments  $^*\text{ZnC}_2\text{H}_5$ ,  $\text{HZnC}_2\text{H}_5$ , and  $\text{ZnH}_2$ .



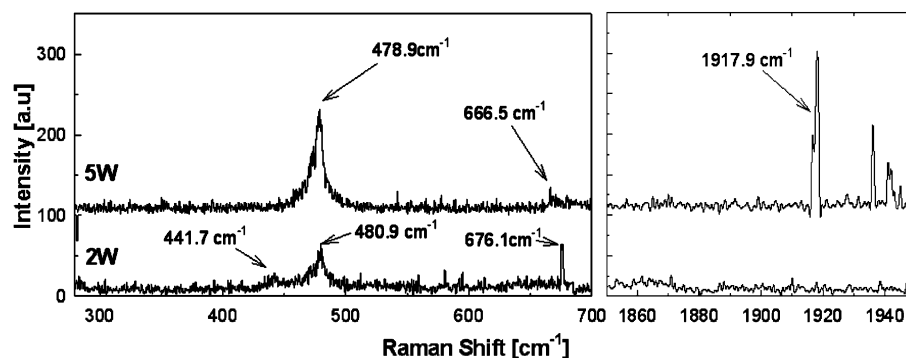


**Figure 2.** Laser-induced Raman shifts of DEZn at room temperature. The lower spectrum was obtained at 1.3 W incident laser power (the laser power setting was 2 W; however, the intensity decreased to 1.3 W incident onto the reactor due to several mirrors placed in the light pathway) and the upper one was obtained at 3.3 W incident laser power.

**3.1. Laser-Induced Decomposition of  $\text{Zn}(\text{C}_2\text{H}_5)_2$  in a Flow Cell.** As presented in the experimental section, room-temperature scattering experiments were performed in the flow cell on DEZn in  $\text{N}_2$  carrier gas to determine the scattering cross-section of DEZn. The literature has suggested both homolysis of the Zn–C bond and  $\beta$ -hydride elimination as the homogeneous decomposition pathway. No reaction intermediates, however, have been experimentally detected for Zn species. The only products detected have been  $\text{ZnH}_2$  and hydrocarbons ( $\text{C}_2\text{H}_4$  and  $\text{C}_2\text{H}_6$ ). In an attempt to evaluate the use of Raman scattering to detect intermediates or products, a series of experiments at high laser power was performed to promote decomposition of DEZn, presumably via photolysis at the 532 nm wavelength of the incident beam. Although the preferred photolysis pathway is not expected to be the same as that for pyrolysis, identification of photolysis decomposition products will assist in the interpretation of the subsequent experiments.

Laser-induced photolysis of a stream of 10 mol %  $\text{Zn}(\text{C}_2\text{H}_5)_2$  in  $\text{N}_2$  nominally at room temperature was studied in the commercial flow cell operating at steady state. No decomposition of  $\text{Zn}(\text{C}_2\text{H}_5)_2$  is expected at low power but as the power is increased photolytic decomposition of DEZn should activate decomposition sufficient to detect reaction intermediates. Because all anticipated fragments reside in the Raman shift ranges 250–700 and 1850–1950  $\text{cm}^{-1}$ , only these ranges were scanned. The Raman spectra obtained for laser powers of 2 and 5 W are shown in Figure 2. The lower spectrum, which was taken at a laser power of 2 W nominal (1.3 W incident) shows a broad vibration peak around 480  $\text{cm}^{-1}$ . Minimal photolysis is anticipated at this incident power and the observed peak is attributed the Zn–C stretch in  $\text{Zn}(\text{C}_2\text{H}_5)_2$ . The main peak assignment was carried out on the basis of the literature as well as computational calculations. It should be noted that all the calculation results in Raman frequencies were also confirmed from values in the literature.<sup>26,30</sup>

Increasing the laser power to 5 W (3.3 W incident) yields an increase in the intensity of the 480  $\text{cm}^{-1}$  band and introduces an additional sharp feature at 1917.9  $\text{cm}^{-1}$ .<sup>26</sup> This feature is attributed to the Zn–H vibrational stretch of  $\text{ZnH}_2$ , consistent with the calculated frequency of 1918.9  $\text{cm}^{-1}$  listed in Table 2. Incomplete decomposition of DEZn and the higher incident power resulted in a strong peak for DEZn. The higher local temperature also produced a peak shift of  $\sim 1$   $\text{cm}^{-1}$  to lower wavelength. A weak scattering signal is detected around at 666.7  $\text{cm}^{-1}$  assigned to the Zn–H symmetrical vibration of  $\text{HZnC}_2\text{H}_5$ . Both of these fragments are expected from decomposition via  $\beta$ -hydride elimination.

The low intensity of the peak corresponding to  $\text{HZnC}_2\text{H}_5$  suggests the second  $\beta$ -hydride elimination is relatively fast

compared to the first  $\beta$ -hydride elimination. It is noted that the peak at 441.7  $\text{cm}^{-1}$  agrees well with the calculated value for Zn–C stretching of the transition-state species in the product of the first  $\beta$ -hydride elimination,  $\text{HZnC}_2\text{H}_5$ . In contrast, no peak was detected in the spectrum at the 5 W power level at the frequency calculated for the homolysis intermediate  $^*\text{ZnC}_2\text{H}_5$ . It is possible, however, that  $^*\text{ZnC}_2\text{H}_5$  radical Raman cross-section is too small for detection or the radical was depleted by subsequent reaction. Identifying hydrocarbon decomposition products would assist in differentiating between the two reaction pathways. The expected hydrocarbon gas molecules, however, have small Raman cross-sectional areas rendering their detection challenging. The detection of  $\text{ZnH}_2$  by Raman scattering in these preliminary experiments suggest that the  $\beta$ -hydride elimination pathway is active at least by photolysis. The results also lend support to the accuracy of the DFT calculations and encouraged the more quantitative study of the pyrolytic decomposition of DEZn using the inverted impinging-jet reactor presented below.

**3.2. Pyrolytic Decomposition of  $\text{Zn}(\text{C}_2\text{H}_5)_2$  in an Inverted Impinging-Jet Reactor.** Given the previously reviewed evidence for both homolysis and  $\beta$ -hydride elimination thermal decomposition pathways, a set of experiments was performed to measure the rate of pyrolysis of DEZn. In these studies,  $\text{Zn}(\text{C}_2\text{H}_5)_2$  was introduced into the center line of the probe reactor depicted in Figure 1 at an inlet concentration 0.5 mol % in  $\text{N}_2$ . The purpose of this experiment was to measure the  $\text{Zn}(\text{C}_2\text{H}_5)_2$  profile along the centerline as well as any other detected reaction products. It is noted that the high temperature reduced the signal-to-noise level, and transverse and axial diffusion diluted the precursor as well as reaction products. The existence of a validated reactor model<sup>25</sup> and rate constants from the computational studies allowed comparison of the experimental profiles to those predicted by the reaction simulation.

The concentration of DEZn was calculated from measured Raman scattering intensities using eqs 3 and 4 and the relative Raman cross-section obtained from the preliminary flow-cell experiments. The intensity ratio of DEZn relative to nitrogen was calculated from eq 4 and mole fraction of DEZn in nitrogen carrier gas was obtained using eq 3 along with the measured temperature gradient. Figure 3 plots the measured centerline DEZn concentration at selected positions below the heated susceptor (set point 600 °C). This figure also shows the temperature profile calculated using a detailed 2-D asymmetrical reactor model. This model is described in greater detail elsewhere, including its validation.<sup>16,25</sup> Briefly, the simulation uses the finite element method (FEM) to simultaneously solve the steady-state momentum, heat, and mass balance equations in a reacting system. It is noted that a  $\sim 160$  °C difference exists between the set-point temperature and the gas-phase temperature

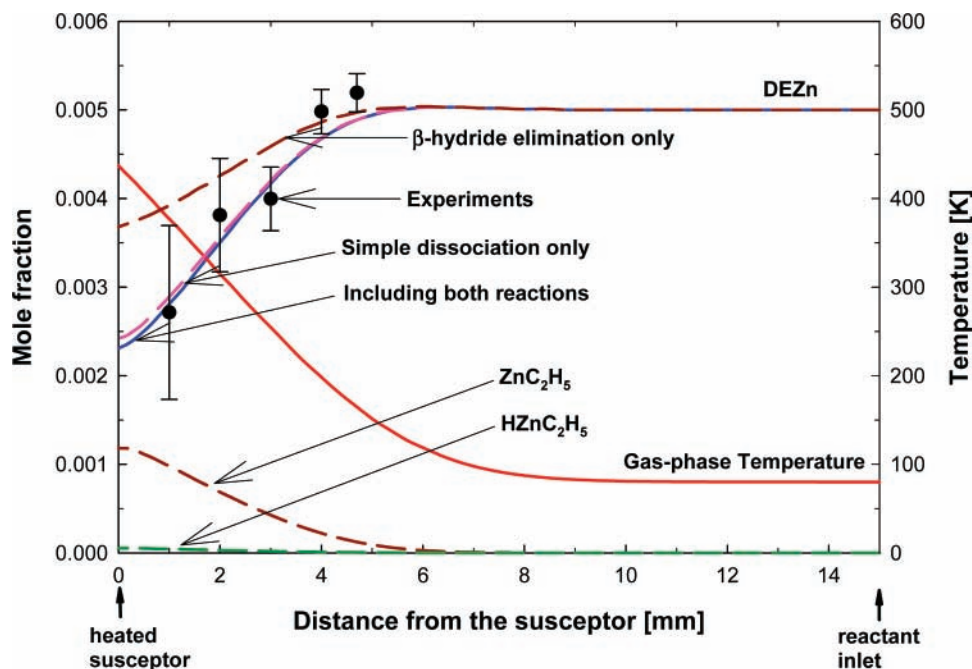


**Figure 3.** Comparison of measured DEZn centerline profile (symbol) to simulated profile assuming only  $\beta$ -hydride elimination (uppermost long dash line) or only homolysis (second uppermost dash line) using the rate constants shown in Table 4. The solid line includes both reactions. The computed profiles of  $\text{ZnC}_2\text{H}_5$  and  $\text{HZnC}_2\text{H}_5$  are also shown with both pathways included.

extrapolated to the heater surface. This difference is a result of thermal resistances between the central thermocouple embedded in the ceramic heater, the glass envelope, and into the gas phase. It is also noted that the thermal boundary layer thickness is on the order of 6 mm at these conditions.

As previously indicated, measurement of the mole fraction of DEZn is challenging because the relative Raman cross-section of the Zn–C stretch is small. It was possible, however, to quantitatively measure the DEZn concentration above a mole fraction of  $\sim 0.5$  mol % as shown in the Figure 3. The onset of DEZn thermal decomposition is seen to occur at  $\sim 4$  mm below the heated susceptor at a gas-phase temperature of  $\sim 150$  °C. The measured profile was compared to that predicted by the reactor model assuming the disappearance of DEZn occurs by homolytic fission using values of  $E_a$  and  $A$  listed in Table 1 by either Koski et al.<sup>11</sup> or Dumont et al.<sup>14</sup>

The comparisons depicted in Figure 3 show that the rate constants suggested by Koski et al.<sup>11</sup> give a lower decomposition extent than using the constants reported by Dumont et al.<sup>14</sup> It is noted that the DEZn profile using the Koski et al. constants is almost identical to that assuming no decomposition occurs. This is because transverse diffusion occurs along the axis to decrease the centerline DEZn concentration and the magnitude of the decrease is similar to the extent homogeneous decomposition. It is also obvious from the comparison that the reported homolysis kinetic data do not fully account for the experimentally observed decomposition extent. It supports the possibility of additional reaction pathways that would lead to increased DEZn decomposition including  $\beta$ -hydride elimination and surface reaction at the quartz plate. If the experimental values are correct, then either the rate constants are incorrect or another decomposition pathway is significant. Table 3 summarizes the calculated reaction rate parameters for both the dissociation and the  $\beta$ -hydride elimination reactions. In rate constant estimation, the basis set super position error (BSSE) correction was considered<sup>27–29</sup> and the calculated rates were well matched with reported rates in Table 1. Figure 3 shows the concentration profiles predicted with these values. As shown in this figure,

**TABLE 3: Calculated Reaction Rate Constants for Homolytic Fission and  $\beta$ -Hydride Elimination<sup>a</sup>**

|                              | $E_a$ [kcal/mol] | $A$ [ $\text{s}^{-1}$ ] |
|------------------------------|------------------|-------------------------|
| homolytic dissociation       | 52.0             | $2.40 \times 10^{17}$   |
| $\beta$ -hydride elimination | 47.2             | $7.90 \times 10^{14}$   |

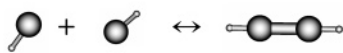
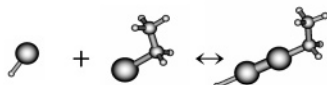
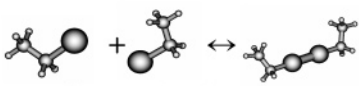
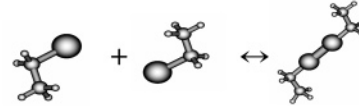
<sup>a</sup> Basis set superposition error (BSSE) correction was considered.

the agreement between experimental concentrations and the predicted profile that includes both pathways is very good. This suggests both  $\beta$ -hydride elimination and homolytic fission occur, with homolysis being the dominant pathway in the temperature range of study.

**3.3. Reaction Intermediates.** The evidence supporting simple dissociation as the preferred pathway includes the observation of the expected final hydrocarbon products (i.e., butane, ethane, and ethane) and a measured apparent activation energy (see Table 1) that is consistent among several investigators and similar to the value suggested by calculations (12). The primary reaction intermediates,  $\cdot\text{ZnC}_2\text{H}_5$  and  $\cdot\text{C}_2\text{H}_5$ , however, have not been detected experimentally, perhaps due to short lifetimes or small scattering cross-sections. In contrast, the observation of solid  $\text{ZnH}_2$  on the cell window during IR laser-powered homogeneous pyrolysis as well as the expected hydrocarbon end products supports the route of double  $\beta$ -hydride elimination. Although the photolysis pathway can be different than the pyrolysis route, it is noted that the single and double  $\beta$ -hydride elimination intermediates  $\text{HZnC}_2\text{H}_5$  and  $\text{H}_2\text{Zn}$  were both observed upon photolysis of DEZn. Thus a series of additional reactions were postulated and the likelihood of their existence probed computationally. The same model chemistry of B3LYP/6-311G(d) was used for consistency to calculate Gibbs energies. In particular, reactions that included  $\cdot\text{ZnC}_2\text{H}_5$  or  $\text{ZnH}$  (possible product from Zn–C bond dissociation of  $\text{HZnC}_2\text{H}_5$ ) were considered.

Table 4 lists four reactions that involve these intermediates that gave negative calculated values of Gibbs energy changes at a reaction temperature of 798.15 °C. Moreover these reactions are exothermic so that the reactions may be facile in the gas

TABLE 4: Favorable Reactions Involving Intermediates Calculated from B3LYP/6-311G(d) Model Chemistry<sup>a</sup>

|   |        |                                   |                                   |
|---|--------|-----------------------------------|-----------------------------------|
| (1) $2 \cdot \text{Zn-H} \leftrightarrow \text{Zn}_2\text{H}_2$                               |        |                                   |                                   |
|              |        |                                   |                                   |
| Raman frequency [Zn-H]: 428.22 cm <sup>-1</sup>   |        |                                   |                                   |
|   | T(K)   | $\Delta\text{H}(\text{kcal/mol})$ | $\Delta\text{G}(\text{kcal/mol})$ |
|   | 398.15 | -31.05                            | -13.18                            |
|   | 498.15 | -31.05                            | -8.69                             |
|   | 598.15 | -31.03                            | -4.20                             |
|   | 698.15 | -31.00                            | 0.29                              |
|   | 798.15 | -30.94                            | 4.76                              |
| (2) $\cdot\text{HZn} + \cdot\text{ZnC}_2\text{H}_5 \leftrightarrow \text{HZnZnC}_2\text{H}_5$ |        | $\Delta\text{H}$                  | $\Delta\text{G}$                  |
|              |        |                                   |                                   |
| Raman frequency [Zn-H]: 434.50 cm <sup>-1</sup>   |        |                                   |                                   |
|   | 398.15 | -35.50                            | -21.25                            |
|   | 498.15 | -35.39                            | -17.68                            |
|   | 598.15 | -35.25                            | -14.14                            |
|   | 698.15 | -35.09                            | -10.62                            |
|   | 798.15 | -34.90                            | -7.13                             |
| (3) $2 \cdot \text{ZnC}_2\text{H}_5 \leftrightarrow (\text{ZnC}_2\text{H}_5)_2$ :cis          |        | $\Delta\text{H}$                  | $\Delta\text{G}$                  |
|              |        |                                   |                                   |
| Raman frequency [Zn-C]: 555.84, 1203.65 cm <sup>-1</sup>                                      |        |                                   |                                   |
|   | 398.15 | -40.01                            | -25.48                            |
|   | 498.15 | -39.75                            | -21.86                            |
|   | 598.15 | -39.46                            | -18.29                            |
|   | 698.15 | -39.14                            | -14.78                            |
|   | 798.15 | -38.81                            | -11.31                            |
| (4) $2 \cdot \text{ZnC}_2\text{H}_5 \leftrightarrow (\text{ZnC}_2\text{H}_5)_2$ :trans        |        | $\Delta\text{H}$                  | $\Delta\text{G}$                  |
|             |        |                                   |                                   |
| Raman frequency [Zn-C]: 555.84, 1203.65 cm <sup>-1</sup>                                      |        |                                   |                                   |
|   | 398.15 | -40.01                            | -24.93                            |
|   | 498.15 | -39.75                            | -21.18                            |
|   | 598.15 | -39.46                            | -17.48                            |
|   | 698.15 | -39.15                            | -13.82                            |
|   | 798.15 | -38.82                            | -10.22                            |

<sup>a</sup> Thermodynamic properties are derived from the same theory level.

TABLE 5: Symmetrical Raman-Active Zn–C or Zn–H Stretching of Zn-Containing Intermediates and Estimated Raman Shifts (cm<sup>-1</sup>) with a Scaling Factor Applied to HZn–ZnC<sub>2</sub>H<sub>5</sub> and (ZnC<sub>2</sub>H<sub>5</sub>)<sub>2</sub><sup>a</sup>

|                | ZnC <sub>2</sub> H <sub>5</sub> ) <sub>2</sub><br>$\nu[\text{Zn-C}]$ | (ZnH) <sub>2</sub><br>$\delta[\text{Zn-H}]$ | HZn–ZnC <sub>2</sub> H <sub>5</sub> |                    | (ZnC <sub>2</sub> H <sub>5</sub> ) <sub>2</sub><br>$\nu[\text{Zn-C}]$ |
|----------------|--|---|-------------------------------------|--------------------|---|
|                |  |   | $\delta[\text{Zn-C}]$               | $\nu[\text{Zn-C}]$ |   |
| calculation    | 486.0  | 428.2                                       | 434.5                               | 548.81             | 1203.7  |
| experiment     | 480.0  |   |                                     |                    | 1185.0  |
| scaling factor | 0.986  | none  | none                                | 0.986              | 0.986   |
| corrected      | 480.0  | 428.2                                       | 434.5                               | 541.1              | 1186.3  |

<sup>a</sup> For Zn–H motions, the correction factor was not adapted.

phase. These reactions include  $2 \cdot \text{Zn-H} \leftrightarrow \text{Zn}_2\text{H}_2$ ,  $\cdot\text{HZn} + \cdot\text{ZnC}_2\text{H}_5 \leftrightarrow \text{HZnZnC}_2\text{H}_5$ , and  $2 \cdot \text{ZnC}_2\text{H}_5 \leftrightarrow (\text{ZnC}_2\text{H}_5)_2$  in both cis- and trans-conformations. Other reactions examined included formation of  $\text{CH}_3\text{ZnC}_2\text{H}_5$ ,  $\text{HZnCH}_3$ , and  $(\text{ZnH})_3$  but the calculated energy changes were positive.

On the basis of the results in Table 4, the most favorable reactions are the monoethylzinc dimerization reactions to form the cis- and trans-conformations. The distance between the two ethyl groups is sufficiently long (6.27 Å) that there should not be a difference in their stability. Therefore, no energy rotation barrier was evident between the cis- and trans-conformations and the Raman-active vibrational frequencies are identical. Table 5 shows the calculated Raman frequencies for each stable reaction intermediate along with the Zn–C symmetrical motions. Given similar Zn–C motions in DEZn and the intermediates

examined, a scaling factor was introduced on the basis of comparison between the experimental and calculated Zn–C vibrational frequencies for DEZn.<sup>30</sup> DFT calculations gave accurate frequency values for the Zn–H stretch, especially for motions containing hydrogen with its symmetrical s orbital.

A second experiment was performed to detect products of reactions between intermediates. In this experiment the susceptor set point temperature was 600 °C to give sufficient decomposition and thus a relatively high concentration of intermediates. The Ar-ion laser power was 1 W and the concentration of DEZn was 0.5 mol % in N<sub>2</sub> carrier gas. On the basis of the calculated Raman shifts shown Table 5, scans were taken over the expanded range 200–1300 cm<sup>-1</sup> (Figure 4). The lower scan was obtained 1 mm above the inlet and the upper scan at 2 mm. The multiple scans increased the signal-to-noise ratio to more confidently extract a value for Raman shift of the intermediate, which likely has a low Raman cross-section.

Comparison of the experimental value of the shift at 1185 cm<sup>-1</sup> to those listed in Table 5 suggests the presence of (ZnC<sub>2</sub>H<sub>5</sub>)<sub>2</sub> as a reaction product of the ZnC<sub>2</sub>H<sub>5</sub> intermediate. In this assignment, the Raman shift of 1185 cm<sup>-1</sup> is not directly attributed to Zn–C vibrational stretching. At first glance, the calculated Raman shift values of Zn–C stretch for DEZn (480 cm<sup>-1</sup>) and (ZnC<sub>2</sub>H<sub>5</sub>)<sub>2</sub> (1185 cm<sup>-1</sup>) does not appear correct. The observed shift at 1185 cm<sup>-1</sup> was detected in a careful scan of the full range. The broad peak shape suggested that the shift

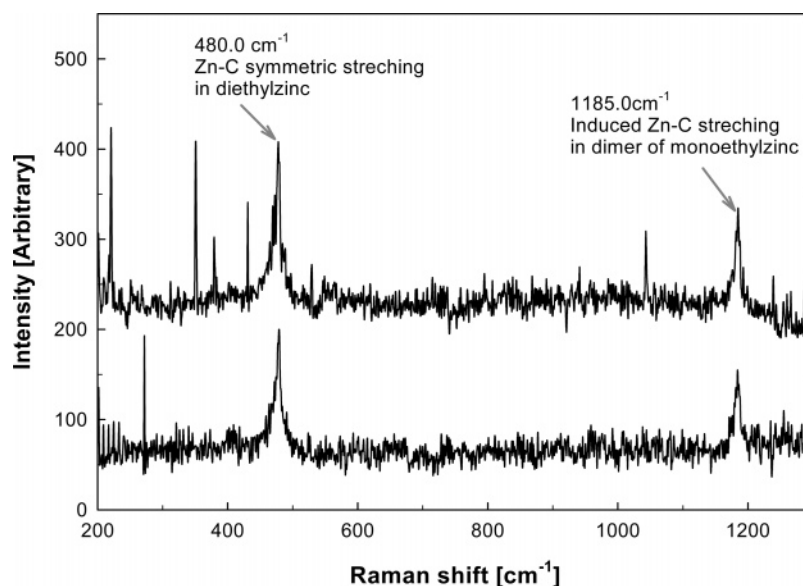


**Figure 4.** Raman spectra at two positions in the reactor (1 and 2 mm above the inlet) indicating presence  $(\text{ZnC}_2\text{H}_5)_2$ .

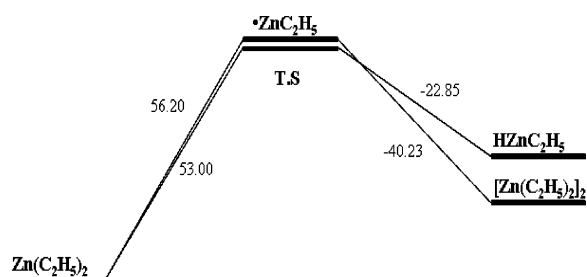


**Figure 5.** Schematic diagram of two suggested competing reactions with reaction enthalpies [kcal/mol] listed.

involved Zn. In an attempt to associate a particular intermediate with this shift, seven intermediate species were screened by DFT. The first screen was on the basis of  $\Delta G$  values, which suggested that  $\text{ZnH}_2$ ,  $\text{HZn-ZnC}_2\text{H}_5$ , and  $(\text{ZnC}_2\text{H}_5)_2$  were thermodynamically likely. Examination of the Zn-C stretching of  $(\text{ZnC}_2\text{H}_5)_2$  using the DEZn scaling factor gave a surprisingly close result. This was rationalized on the basis that the Zn-C-C angle is calculated as  $116^\circ$  rather than  $90^\circ$ . Because the Zn-C stretching was induced by the C-C stretching motion, the relative Raman cross-section was expected to be small. Therefore, the actual detection of this peak was challenging and was only possible by using multiple scans and long integration times. On the basis of experimental observations and support from DFT calculations, the thermal decomposition of DEZn has energies as depicted in Figure 5.

#### 4. Conclusions

The decomposition pathways of  $\text{Zn}(\text{C}_2\text{H}_5)_2$  were investigated by both Raman spectroscopy and DFT calculations at the B3LYP/6-311G(d) chemistry level. With the aid of the DFT calculations the species formed during laser-induced photolysis could be identified as  $\text{HZnC}_2\text{H}_5$  (minor species) and  $\text{H}_2\text{Zn}$  (major species). This gives support for including  $\beta$ -hydride elimination as a photolytic reaction pathway. During pyrolysis, however, these species were not detected, suggesting  $\beta$ -hydride elimination is not dominant in this mode. As summarized below, the dimer  $(\text{ZnC}_2\text{H}_5)_2$  was observed during pyrolysis, and although not a direct decomposition product, its detection supports homolysis as the dominant DEZn thermal decomposition pathway. The thermal decomposition of DEZn was followed

in an up-flow impinging-jet reactor using Raman scattering and following the  $480\text{ cm}^{-1}$  line attributed to symmetrical stretch of the Zn-C bond. The Raman shift for the diethylzinc species was confirmed using the B3LYP/6-311G(d) model chemistry. The measured concentration profile was then compared to those predicted by a 2-D hydrodynamic simulation including various rate equations. This comparison indicates that homolytic fission of the Zn-C bond is the dominant initial reaction, although  $\beta$ -hydride elimination is also active. The reaction intermediate  $^*\text{ZnC}_2\text{H}_5$  does not have a sufficient lifetime to be detected and secondary products such as ethane, ethane, and butane have very low cross-sections and are thus also difficult to detect using Raman spectroscopy. The dimerization of the reaction intermediate  $\text{ZnC}_2\text{H}_5$  was confirmed both by experiment and by DFT calculations. Consequently, the dissociation of DEZn and a second minor  $\beta$ -hydride elimination reaction were identified as likely pathways in the presented research. The agreement between the calculated Raman shifts and the experimentally observed shifts is remarkable and provides evidence for the benefits of combining DFT calculations and experiments.

#### References and Notes

- (1) Waag, A.; Gruber, Th.; Thonke, K.; Sauer, T.; Kling, R.; Kirchner, C.; Röss, H. *J. Alloy Compd.* **2004**, *371*, 77.
- (2) Wang, L.; Pu, Y.; Chen, Y. F.; Mo, C. L.; Fang, W. Q.; Xiong, C. B.; Dai, J. N.; Jiang, F. Y. *J. Cryst. Growth* **2005**, *284*, 459.
- (3) Bachari, E. M.; Baud, G.; Ben Amor, S.; Jacquet, M. *Thin Solid Films* **1999**, *348*, 165.
- (4) Cho, S.; Ma, J.; Ki, Y.; Sun, Y.; Wong, G. K. L.; Ketterson, J. B. *Appl. Phys. Lett.* **75** (18), 2761.
- (5) Haga, K.; Katahira, F.; Watanabe, H. *Thin Solid Films* **1999**, *343*, 145.
- (6) Mycielski, A.; Kowalczyk, L.; Szadkowski, A.; Chwalisz, B.; Wyszomolek, A.; Stepniowski, R.; Baranowski, J. M.; Petemski, M.; Witowski, A.; Jakiela, R.; Barcz, A.; Witkowska, B.; Kaliszek, W.; Jedrzejczak, A.; Suchocki, A.; Lusakowska, E.; Kaminska, E. *J. Alloy Compd.* **2004**, *371*, 150.
- (7) Li, X.; Yan, Y.; Gessert, T. A.; DeHart, C.; Perkins, C. L.; Young, D.; Coultts, T. J. *Electrochem. Solid State Lett.* **2003**, *6* (4), C56.
- (8) Ghandi, S.; Field, R.; Shealy, J. *Appl. Phys. Lett.* **1980**, *37* (5), 449.
- (9) Look, D. C.; Reynold, D. C.; Litton, C. W.; Jones, R. L.; Eason, D. B.; Cantwell, G. *Appl. Phys. Lett.* **2002**, *81* (10), 1830.
- (10) Minegishi, K.; Koiwai, Y.; Kokuchi, Y.; Yano, K. *Jpn. J. Appl. Phys.* **1997**, *36*, L1453.
- (11) Koski, A. A.; Price, S.; Trudell, B. C. *Can. J. Chem.* **1976**, *54*, 482.
- (12) Jackson, D. A., Jr. *J. Cryst. Growth.* **1989**, *94*, 459.



- (13) Dumont, H.; Marbeuf, A.; Bouree, J. E.; Gorochov, O. *J. Mater. Chem.* **1992**, 2 (9), 923.
- (14) Dumont, H.; Marbeuf, A.; Bouree, J. E.; Gorochov, O. *J. Mater. Chem.* **1993**, 3 (10), 1075.
- (15) Linney, R. E.; Russell, D. K. *J. Mater. Chem.* **1993**, 3 (6), 1587.
- (16) Hwang, J. Y.; Park, C.; Huang, M.; Anderson, T. *J. Cryst. Growth* **2005**, 279, 521.
- (17) Long, D. A. *Raman Spectroscopy*; McGraw-Hill: New York, 1977.
- (18) Schrötter, H. W.; Klöckner, H. W. In *Raman Spectroscopy of Gases and Liquids*; Weber, A., Ed.; Springer-Verlag: New York, 1979; Chapter 4.
- (19) Jackson, R. L. *J. Chem. Phys.* **1992**, 96 (8), 5938.
- (20) Frisch, M. J.; Trucks, G. W.; Schlegel, H. B.; Scuseria, G. E.; Robb, M. A.; Cheeseman, J. R.; Montgomery, J. A., Jr.; Vreven, T.; Kudin, K. N.; Burant, J. C.; Millam, J. M.; Iyengar, S. S.; Tomasi, J.; Barone, V.; Mennucci, B.; Cossi, M.; Scalmani, G.; Rega, N.; Petersson, G. A.; Nakatsuji, H.; Hada, M.; Ehara, M.; Toyota, K.; Fukuda, R.; Hasegawa, J.; Ishida, M.; Nakajima, T.; Honda, Y.; Kitao, O.; Nakai, H.; Klene, M.; Li, X.; Knox, J. E.; Hratchian, H. P.; Cross, J. B.; Bakken, V.; Adamo, C.; Jaramillo, J.; Gomperts, R.; Stratmann, R. E.; Yazyev, O.; Austin, A. J.; Cammi, R.; Pomelli, C.; Ochterski, J. W.; Ayala, P. Y.; Morokuma, K.; Voth, G. A.; Salvador, P.; Dannenberg, J. J.; Zakrzewski, V. G.; Dapprich, S.; Daniels, A. D.; Strain, M. C.; Farkas, O.; Malick, D. K.; Rabuck, A. D.; Raghavachari, K.; Foresman, J. B.; Ortiz, J. V.; Cui, Q.; Baboul, A. G.; Clifford, S.; Cioslowski, J.; Stefanov, B. B.; Liu, G.; Liashenko, A.; Piskorz, P.; Komaromi, I.; Martin, R. L.; Fox, D. J.; Keith, T.; Al-Laham, M. A.; Peng, C. Y.; Nanayakkara, A.; Challacombe, M.; Gill, P. M. W.; Johnson, B.; Chen, W.; Wong, M. W.; Gonzalez, C.; Pople, J. A. *Gaussian 03*, revision C.02; Gaussian, Inc.: Wallingford, CT, 2004.
- (21) Simka, H.; Willis, B. G.; Lengyel, I.; Jensen, K. F. *Prog. Cryst. Growth Charact.* **1997**, 35, 117.
- (22) Smith, S. M.; Schlegel, H. B. *Chem. Mater.* **2003**, 15, 162.
- (23) Nagel, V. B.; Bruser, W. *Z. Anorg. Allg. Chem.* **1980**, 468, 148.
- (24) Corliss, C. H.; Bozman, W. R. *Experimental Transition Probabilities for Spectral Lines of Seventy Elements*; National Bureau of Standards monograph; NBS: Washington, DC, 1962; p 53.
- (25) Hwang, J. Y.; Park, C.; Huang, M.; Anderson, T. *J. Electrochem. Soc.* **2005**, 152 (5), C334.
- (26) Wang, X.; Andrews, L. *J. Phys. Chem. A* **2004**, 108, 11006.
- (27) Kim, Y. S. Ph.D. dissertation, Chemical Engineering, University of Florida, 2007.
- (28) Pelekh, A.; Carr, R. W. *J. Phys. Chem. A* **2001**, 105, 4697.
- (29) Duijneveldt, F. B.; Duijneveldt-van Rijdt, J. G. C. M.; Lenthe, J. H. *Chem. Rev.* **1994**, 97 (7), 1873.
- (30) Park, C. H.; Zhang, S. B.; Wei, S. H. *Phys. Rev. B* **2002**, 66, 073202.